Hypervelocity impact testing on stochastic and structured open porosity cast Al-Si cellular structures for space applications

R. Voillat[a,*], F. Gallien[a,b], A. Mortensen[b], V. Gass[a,**]

[a] *EPFL Swiss Space Center, PPH 338, Station 13, CH-1015 Lausanne*
[b] *EPFL Laboratory of Mechanical Metallurgy, MX-D 141, Station 12, CH-1015 Lausanne*

Abstract

A hypervelocity (6.7–7.0 km/s) impact testing campaign was conducted using Ø 2 mm, 95% Al projectiles onto A357 aluminium alloy stochastic foams with 4-5 mm typical pore dimensions, or alternatively diamond cubic periodic structures of cast AlSi12 with a 6 mm lattice parameter, in order to assess their performance as shielding material against orbital impacts. Either 0.15 mm Al foil or multi-layer insulation (MLI) was used as a front bumper material.

It was found that the periodic structures failed to retain the impact debris for any incident angle of impact between 0° and 12°, at least in part due to ricochets and/or spalled material finding its way through open straight channels within the periodic structure. A porous material architecture traversed by no open, straight path is thus required for proper impact protection. Stochastic foams satisfy this criterion and indeed were found to stop the debris. Depending on bumper configuration, stochastic foams gave comparable performance to that of simple Whipple shield designs at 1.3–1.9× the areal weight. We suggest that a finer pore structure with respect to the projectile diameter should yield a higher impact absorption per areal weight.

As an auxiliary result, it was found that MLI as a front bumper was less efficient in fragmenting the projectile compared to Al foil of similar areal weight.

In conclusion, open porosity stochastic foams are a promising material as sandwich panel cores for space applications, as they may reduce the need for a dedicated shield, so long as the small debris produced by the impact can be isolated from the satellite systems.

*Corresponding author
**Principal corresponding author

Contents

Nomenclature

Acronyms & abbreviations

BLE Ballistic Limit Equation

HVIT Hypervelocity Impact Testing

LEO Low Earth Orbit

PS Periodic Structure

SF Stochastic Foam

WS Whipple Shield

Mathematical symbols

ρ mass density (g/cm^3)

σ yield strength (ksi)

θ incident angle

c speed of sound in material (km/s)

d projectile diameter (cm)

f_s solid volume fraction

H Brinell hardness (HB)

S standoff distance (cm)

t thickness (cm)

V velocity (km/s)

Subscripts

b bumper

c critical

t target

w rear wall

1. Introduction

In light of the ever growing number of Low Earth Orbit (LEO) inert objects, orbital collisions pose a significant risk to current operational satellites. In 1978, the densification of LEO space junk led NASA scientists Donald J. Kessler and Burton G. Cour-Palais to suggest a catastrophic scenario named the Kessler Syndrome, whereby a cascading effect of collisions may exponentially increase the total count of independent debris (without affecting the total mass), prohibiting any space operation on entire orbital levels for years, apart from launches of trajectory extending past those levels.

This has motivated a strong effort to mitigate the number of debris, via scheduled End-of-Life operations on new orbiting objects (by de-orbiting or migrating to so-called graveyard orbits), or the developement of reusable rocket stages[1] [2]. Another implication of the increasing number of LEO inert objects is that there is now a strong incentive to protect new spacecrafts against manageable impacts, occuring at velocities between 2–77 km/s. This has led to the development of what is now known as Hyper-Velocity Impact Testing (HVIT), a testing procedure initated in the mid-20$^{\text{th}}$ century.

Initial HVIT testing campaigns quickly led to the conclusion that monolithic shields are inefficient in terms of energy dissipation per areal mass, motivating the search for alternative low-weight materials solutions to mitigate the effect of collisions with LEO inert objects. In a review of the extensive HVIT leading up to the Apollo missions, Cour-Palais proposed in 1987 a set of equations for the penetration depth of spherical projectiles into metal [1]. For a semi-infinite target, the penetration depth P_∞ if $\rho_p/\rho_t < 1.5$ and $3 \leq V \leq 8$ km/s (see nomenclature for symbol definitions and units) is given by

$$P_\infty = 5.24\ d^{19/18}\ H_t^{-0.25}\ (\rho_p/\rho_t)^{0.5}\ (V_n/c)^{2/3} \tag{1}$$

On that basis, empirical Ballistic Limit Equations (BLE) were introduced in 1993 by E. L. Christiansen at the NASA Johnson Space Center [2], by fitting HVIT data on Al Whipple shields. For a simple Whipple shield – a front bumper with a single rear wall – in 3 velocity regimes, the critical debris diameter for a given shield design is given by :

[1] http://www.esa.int/Our_Activities/Space_Engineering_Technology/Clean_Space/Developing_anti-space_debris_technologies

[2] https://gsp.esa.int/articles/-/wcl/lGnxp6cuQgi6/10192/end-of-life-disposal-of-satellites

$$V < 3 \text{ km/s:} \quad d_c = \left(\frac{t_w (\sigma_w/40)^{0.5} + t_b}{0.6\,(\cos\theta)^{5/3} \rho_p^{0.5} V^{2/3}} \right)^{18/19} \tag{2}$$

$$\begin{aligned} 3 \leqslant V \leqslant 7 \text{ km/s:} \quad d_c = \; & \frac{7 - V\,\cos\theta}{4} \times \left(\frac{t_w\,(\sigma_w/40)^{0.5} + t_b}{1.248\,\rho_p^{0.5}\,\cos\theta} \right)^{18/19} \\ & + \frac{1.071\,V\,\cos\theta - 3}{4} \times \left(\frac{t_w^2\,S\,\sigma_w}{70\,\rho_p\,\rho_b^{1/3}} \right)^{1/3} \end{aligned} \tag{3}$$

$$V > 7 \text{ km/s}: \quad d_c = 3.918 \left(\frac{t_w^2\,S\,\sigma_w}{70\,\rho_p\,\rho_b^{1/3}\,(V\,\cos\theta)^2} \right)^{1/3} \tag{4}$$

where $[\sigma_w] = \text{ksi}$, $[\rho] = \text{g}/cm^3$, $[V] = \text{km/s}$, and $[d_c] = [t] = [S] = \text{cm}$. While Whipple shields provide a weight-efficient protection against a certain rage of hypervelocity impacts, they are bulky and lack other functional properties.

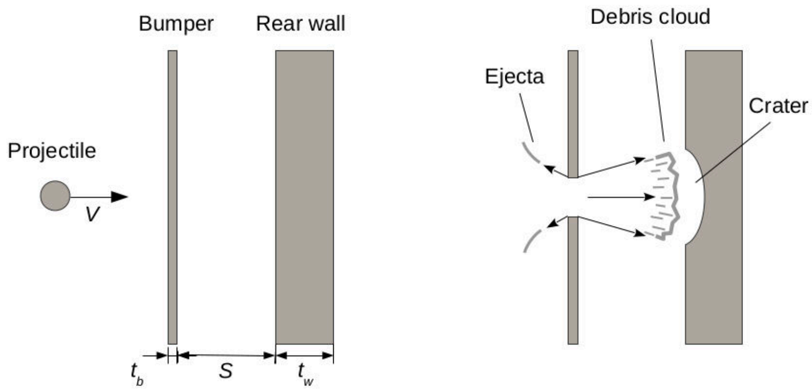

Figure 1.1: Simple Whipple shield design and impact phenomena.

An alternative approach is to use a porous metallic structure to protect satellites from in-orbit collisions with space debris. Porous metals come in several forms [3][4]. For space applications, closed pore structures have the disadvantage that they trap gas; this makes open-pore structures more attractive despite their lower strength or stiffness. Open-pore metal structures, in turn, come in two classes, namely (i) irregular, stochastic foam (SF) structures, or (ii) periodic structures (PS). Both of these open pore metal types can nowadays be produced using several possible methods, and have other advantages than their comparatively low density; for example, they may also serve as high surface area heat exchanger for satellite thermal control, making them attractive potential materials for satellite protection against debris collision.

The HVIT performance of aluminium honeycomb sandwich panels was described by Gehring in

1970, revealing the channeling effect of the open hexagonal channels, leading to poor protection against impacts of normal incidence [5]. Their performance was later compared against open-pore aluminium foam cores panels by Yasensky in 2008 [6] and Ryan *et al.* in 2009 [7] and 2015 [8], demonstrating the superior inherent protection offered by metal foams against HVI at any incident angle.

We present here a study in which the performance of each of these two types of open-pore metal is tested for its HVI behaviour, comparing also the front bumper performance of Multi-Layer Insulation (MLI) over monolithic Al sheets of similar areal weight. As will be seen, the comparative performance of these two materials is, in the context of HVIT performance, the inverse of what is generally found for basic mechanical properties such as stiffness or strength: here, the stochastic structure outperforms the regular, topologically optimized structure.

2. Material and methods

2.1. Open porosity sample material

Two types of open-pore aluminium cellular structures were used in this work:

1. Stochastic metal foams (SF; note that we follow usual practice of calling such materials a foam, even though they were not produced by foaming) of aluminium casting alloy A357, produced under the tradename "Corevo" by the Constellium company (Ussel, France) using the replication method, in which the molten aluminium alloy is infiltrated into a sacrifical salt template, and solidified before leaching away the template. The average SF density was measured at $\rho_{foam} = 0.55 \pm 0.05\,\mathrm{g\,cm^{-3}}$ corresponding to an Al solid volume fraction (or relative density) $f_S^{foam} = 20.9 \pm 1.8\%$. Typical wall-to-wall distances within pores are in the range $3 - 5$ mm.
2. Periodic structures (PS) of Al-12wt. pct. Si were produced at EPFL by precision casting the alloy into a mould having a cavity produced by a 3D printed pattern of organic material, again removing the mould after solification of the metal. By design, the structure is that of a diamond cubic (DC) array of nodes interconnected by cylindrical rods. The lattice parameter is $a = 6$mm and the rod diameter was roughly $\varnothing 1.7 \pm 0.03$mm. The average density of PS was measured at $\rho_{struct} = 0.89 \pm 0.02\mathrm{g\,cm^{-3}}$ corresponding to a metal volume fraction $f_S^{struct} = 33.5 \pm 0.9\%$. These structures have open, square channels between each unit cell column, running in the three $< 100 >$ directions. The channels were a little over 2 ± 0.1mm in side length. Narrower straight open channels extending across the PS material are also found in the $< 110 >$ directions.

All samples were cut into $36 \times 36 \times 48$ mm rectangular prisms. For stochastic foams, this was accomplished using electrical discharge machining (EDM). The PS were already cast into $6 \times 6 \times 8$

cubes of 6 mm side length, so only the sprues and other casting features had to be removed using a hacksaw and a belt sander.

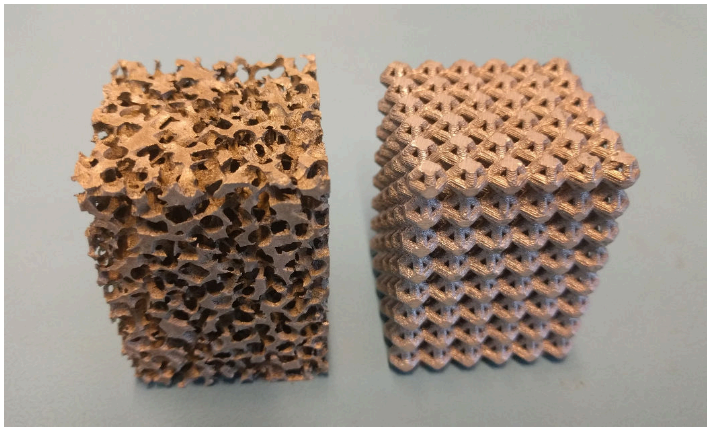

Figure 2.1: Left: stochastic foam sample. Right: structured diamond samples.

The bumper material was also of two types:

1. 98-99,5% Al foil, $t = 0.15\,\text{mm} \pm 6\%$ as per BS EN 546-3 standard for foil dimensions (confirmed by optical microscopy), weighed at 0.041 ± 0.001 g/cm$^{\mathbf{2}}$. The choice of a 0.15 mm thickness is justified by a $t/D = 0.075$ ratio between bumper thickness and bumper projectile – below the regime transition in debris cloud spread at $t/D \approx 0.15$, as described in [9] – so as to observe a worst-case scenario for the debris cloud spread. This material was provided by Braun Metall GmbH, 76676 Graben-Neudorf, Germany.
2. Space-qualified Multi-Layer Insulation (MLI) consisting of 10 layers of 13 μm-thick PET film, coated on both sides by Vacuum Deposited Aluminium (VDA). The films are separated by layers of a proprietary mix of non-woven ceramic fibres, averaging 14–15 g/m$^{\mathbf{2}}$in areal density. The total areal mass of MLI was weighed at 0.035 ± 0.001 g/cm$^{\mathbf{2}}$. This material was provided by courtesy of RUAG Space GmbH, 3000 Bern, Switzerland.

Araldite® Standard ambient curing two-component epoxy adhesive was used for any glueing operation of metal on metal.

2.2. Projectile and target configurations

A total of 8 hypervelocity impacts were scheduled for the testing campaign, using for all a ⌀2 mm, 95% Al sphere, travelling between 6.5–7.1 km/s. At 7.0 km/s, this 11.3 mg projectile has a momentum of $0.079\text{kg}\,\text{m}\,\text{s}^{-1}$ and a kinetic energy of 276.4 J.

The following parameters defined the 8 different test configurations:

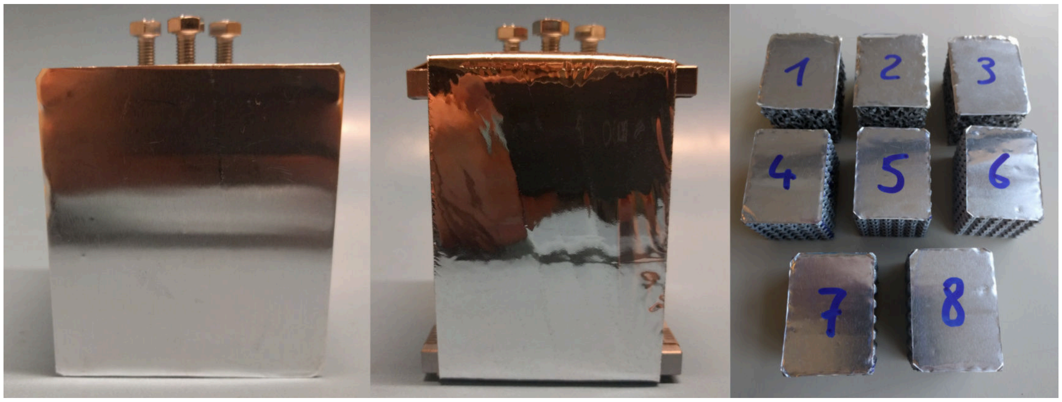

Figure 2.2: Before impact (left to right): Foil bumper, MLI bumper, rear skins.

1. Core material: SF or PS
2. Bumper material: 0.15 mm Al foil or MLI
3. Bumper spacing (= the distance between the bumper and the face of the core along the projectile's trajectory): 0 mm or 10 mm
4. Core orientation (= the angle between the face of the core and the bumper): 0° (parallel) or 12°

Table 2.1 summarizes the eight test configurations.

Table 2.1: Target configurations. Volume fraction derived from weight measurements.

Target	**Core**	$f_S^{core}(\pm\ 0.2\%)$	**Bumper**	**Spacing**	**Orientation**
1	SF	20.3%	Al foil	against	0°
2	SF	19.8%	Al foil	10 mm	0°
3	SF	23.5%	MLI	10 mm	0°
4	PS	34.8%	Al foil	against	0°
5	PS	32.2%	Al foil	10 mm	0°
6	PS	33.2%	Al foil	10 mm	12°
7	PS	32.6%	MLI	10 mm	0°
8	PS	33.6%	MLI	10 mm	12°

In all configurations, the angle of incidence of the projectile with respect to the normal to the bumper was 0° (perpendicular). This value was chosen to ensure that the debris cloud shape would be the same across all tests, such that only the effect of core orientation would be observed for each sample. Because they do not have principal directions, with stochastic foams (SF) there should be no influence of core orientation; hence, it was decided that all stochastic targets were to be tested only with a 0° core orientation. The 12° orientation angle for periodic structure (PS) targets was chosen because it obscured any direct line of sight between the front and the back of the structure, leading to

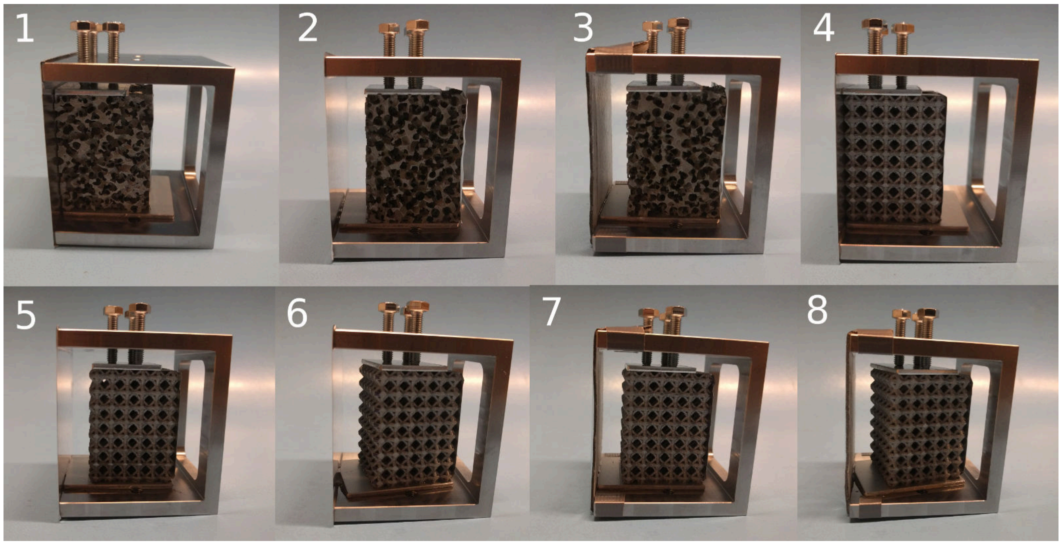

Figure 2.3: 8 different target configurations, ready for testing.

expect that this would suffice to contain the debris cloud entirely in case of a direct hit into an open channel.

Each target core had an 0.15 mm Al foil skin glued to its rear face, as a witness in case of complete penetration by the debris cloud. The front bumper was not glued onto the face of the core of targets with no spacing.

An extra 0.76 ± 0.01 mm thick Al witness plate was attached against the back of each sample holder using tack tape, for it to receive any potential debris making it through the rear skin.

2.3. Testing apparatus

The two-stage light gas gun used to launch the ⌀2 mm Al spheres was designed, built and operated by Thiot Ingénierie in their testing facilities in Puybrun, France. Nicknamed "Hermes", it was set up for a launch using a ⌀5 mm barrel and He gas. In this Hermes testing rig, the first stage operates using compressed gas at 30 MPa and a fast-release valve rather than pyrotechnics. A polymer sabot is used to launch the projectile; it is separated and stopped using a 15–20 mm thick steel plate in front of the target. A ⌀12 mm hole is drilled into the plate to leave a passage for the Al projectile. Residual air pressure is required in the chamber to separate the sabot, so a low-medium vacuum on the order of 10^{-3} torr is pulled (this is $10^7\times$ greater than in LEO).

The integrity of the projectile is assessed using RX flash photography. The velocity is measured at the muzzle using a Tektronix TDS5054 oscilloscope to read optical laser barriers. Infrared high speed photographs are taken using a Phantom® v2012 set to 340 000 FPS, on a 20–25 mm field of view

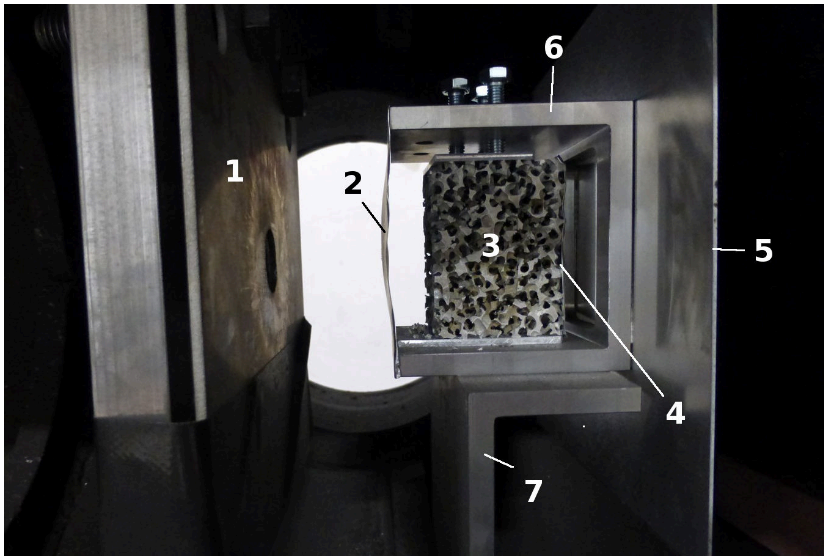

Figure 2.4: Test chamber configuration (Sample 2, after impact). 1: Stop plate, 2: bumper, 3: core, 4: rear skin, 5: witness plate, 6: C-support, 7: L-adapter.

around the point of impact. The camera is set to one side of the target, which is illuminated from the opposite side using an IR 810 nm laser. Images are captured at 810±6 nm through a band-pass filter.

2.4. Target holder

The cores were clamped into C-shaped steel supports using $3 \times$ M5 screws pressing against the top surface of the sample. Each screw was tightened to a light $20 \pm 1\,\mathrm{cN\,m}$ torque value, so as not to apply excess compressive load in case the core was to be structurally deteriorated in testing. A drop of epoxy glue was added at the base of each screw, to prevent/reveal any unexpected loosening of the screws during shipping and testing.

A window was cut in the back of the C-support to allow any residual debris to pass through and be collected onto an Al witness plate. A dab of epoxy adhesive was applied between the core and C-support, to ensure there would be no slippage during shipping and testing. One of the assembled targets is shown in Fig. 2.6.

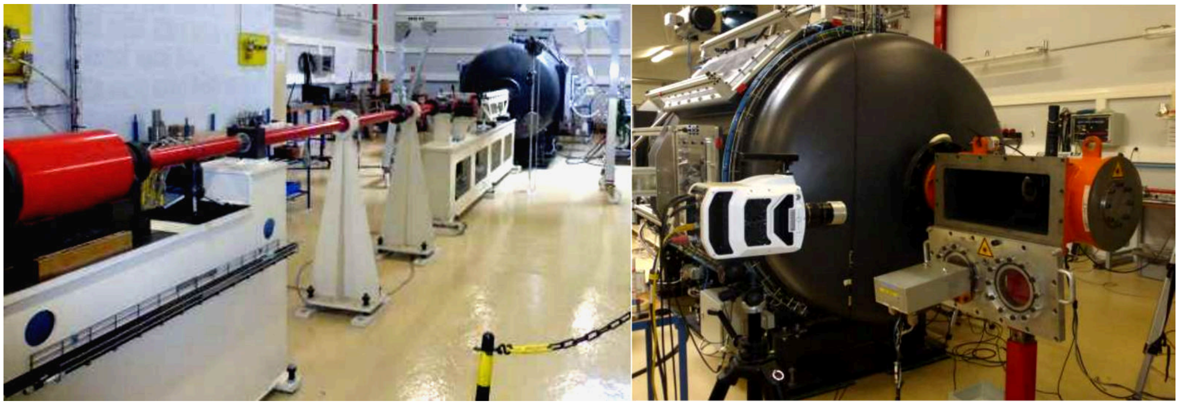

Figure 2.5: *Hermes* two-stage light gas gun (left) and the test chamber (right). The Phantom v2012 camera used for ultrahigh speed photography is visible, filming from the right-hand side of the impact trajectory. Courtesy of Thiot Ingénierie.

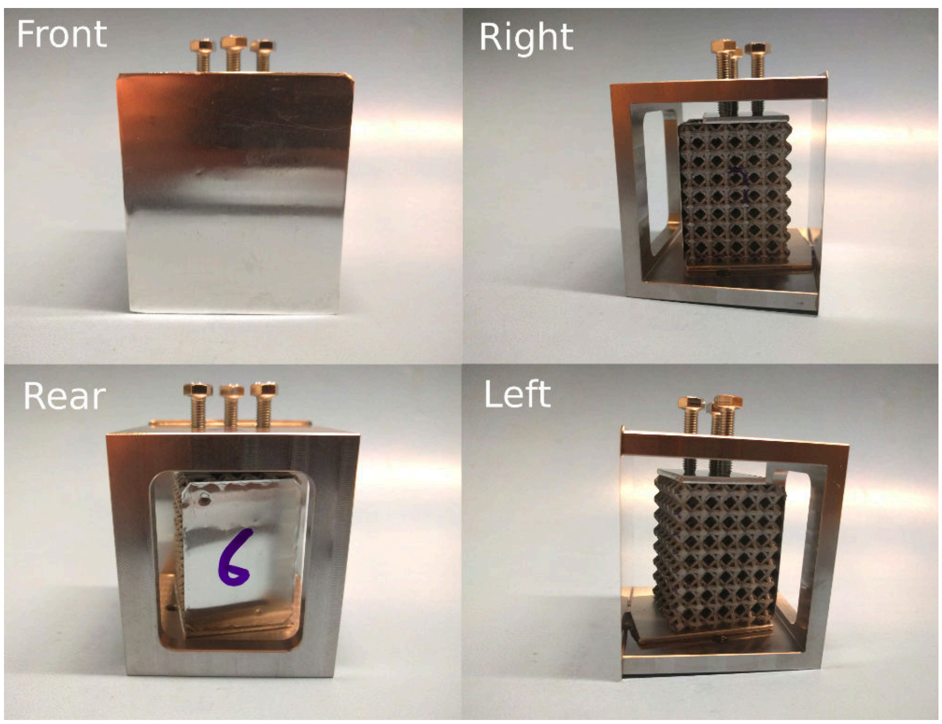

Figure 2.6: Target 6 (PS, foil bumper, 10mm spacing, 12° angle) ready to be mounted onto the L-adapter.

2.5. CT scans

After testing, each (”post-mortem”) sample was examined by X-ray Computed Tomography (CT) scanning at ESTEC (ESA facilities, Noordwijk, The Netherlands) using a Phoenix v—tome—x m300 apparatus (GE Sensing & Inspection Technology GmbH), so as to produce a 3D picture of the remaining material structure. More specifically, Samples 1,2, 3–6 went through a lower resolution (75

Table 2.2: Summary of CT scan configurations

Sample	Config.	Res. (μm/voxel)	kVp	Current (mA)	Acqu. time (ms)
1	full	74.4	260	200	500
	HD	29.9	230	60	1000
2	full	74.7	260	200	333
	HD	29.4	230	60	1000
3	HD	29.9	230	60	1000
4	full	74.4	260	200	500
	HD	29.9	230	60	1000
5	full	74.5	260	200	333
	HD	29.8	230	60	1000
6	full	75.6	260	200	500
	HD	29.9	230	60	1000
7	HD	30.0	230	60	1000
8	HD	30.0	230	60	1000

μm/voxel) scan, so as to capture the front bumper. Due to density mismatches between the polymer/ceramic MLI, Al-Si core and steel C-support, Targets 3, 7 and 8 were not submitted to the low-resolution scan. Then a higher (30 μm/voxel)resolution scan was performed on the cores alone for all eight samples. The scan configurations are summarized in Table 2.2.

2.6. Optical microscopy

In order to determine the effect of the impact onto the microstructure and to map the affected regions within the sample, a metallurgical microscopy study was conducted. Target 2 as representative of SF structures and Target 6 for PS structures were selected for the analysis. The samples were cut using electrical discharge machining, embedded in Epofix^{TM} two-component, clear epoxy resin, ground using a sequence of 120, 180 and 320 grit emery paper, and polished using 3 μm and 1 μm diamond suspension.

On the PS target, all images were obtained from a Zeiss Axioplan 2 optical microscope with coaxial illumination, without using a bandwidth filter. On the SF target, the images were obtained from a Keyence VHX-5000 optical microscope at 20–200× magnification; here, the illumination was a combination of coaxial and right diffuse light. At 700× magnification, we used coaxial illumination alone.

3. Results & discussion

3.1. Bumper behaviour

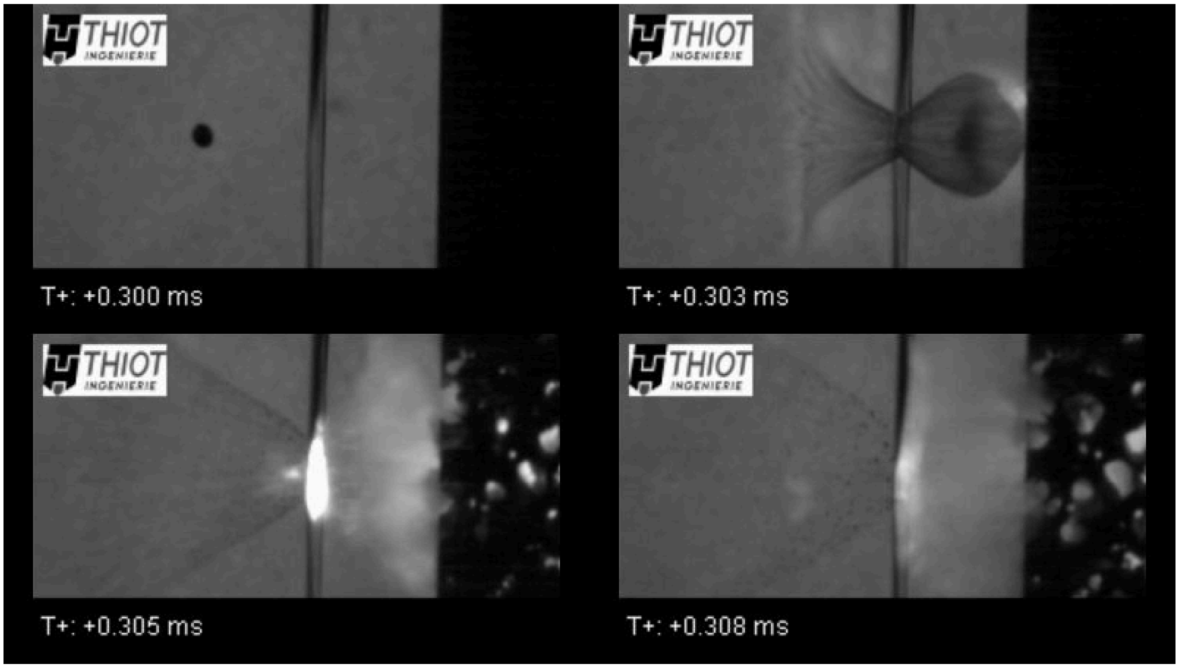

Figure 3.1: Impact on Target 2 – 0.15 mm Al foil bumper, 10 mm spacing, SF – $v = 6948$ m/s

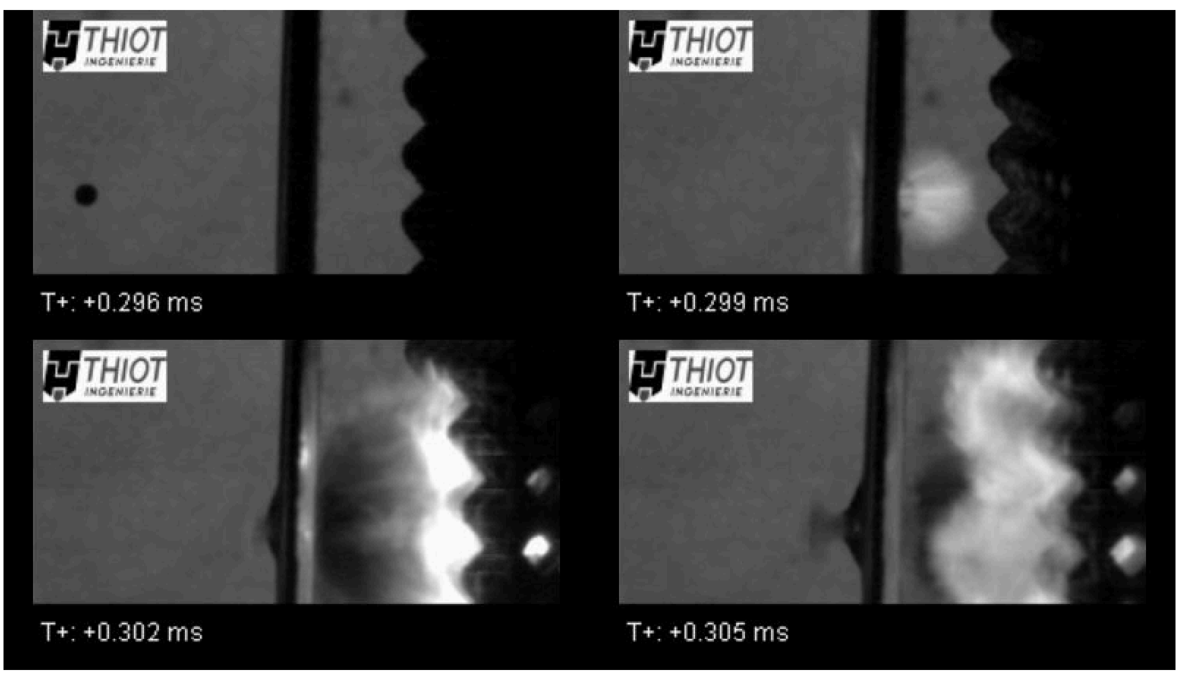

Figure 3.2: Impact on Target 8 – MLI, 10 mm spacing, PS at 12° – $v = 7025$ m/s

From the high-speed photograph on Fig. 3.3, we can deduce that the dispersion angle of the debris cloud exiting the 0.15 mm Al foil, has an overall angular spread of at least 16°, consistent with predictions from [9]. From the low contrast, low resolution photograph alone, one is tempted to extend the dispersion of the central debris cloud to an angle of 30°; however, no significant damage was found beyond 17°on all samples. The cloud of expelled material surrounding the central fragment cloud extends up to 61°.

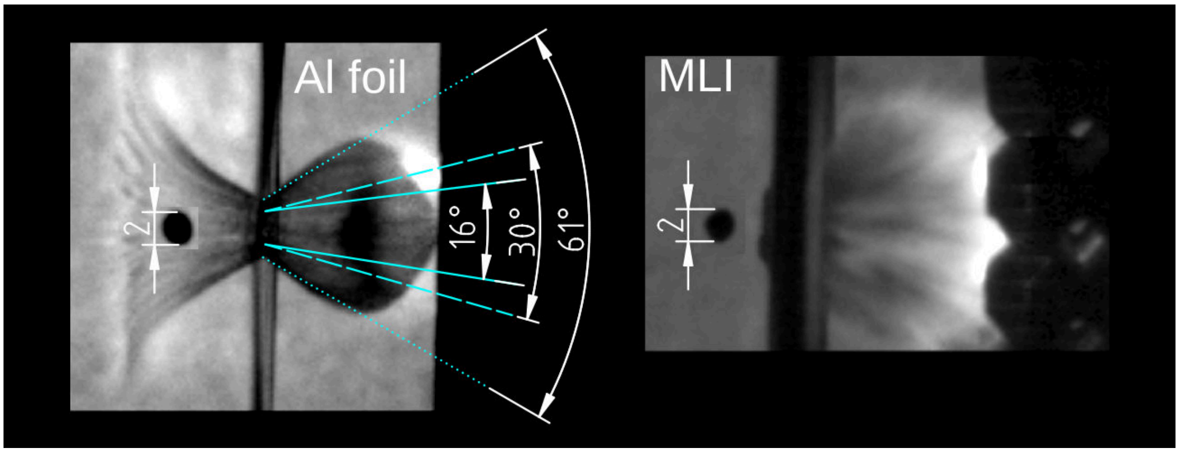

Figure 3.3: Debris cloud measurements on composite images showing the projectile before and after impact against the bumper. Left: impact on 0.15 mm Al foil, taken during impact on Target 2, with a range of dispersion for the central fragment. Right: impact on MLI, taken from Target 8. The central fragment is obscured by the cloud, such that no relevant measurement on dispersion can be made.

Impacts on MLI produced too much organic dust to be properly analysed using data from the high-speed camera; however, affected areas within the samples suggest that the cloud of debris from the destruction of the foil material itself is also contained within an angle 15° wide. Despite a standoff distance of 10 mm between the MLI and SF core in Target 3, the crater was found to be narrower and as deep as in Target 1, where the front bumper is against the SF core. Moreover, PS Target 8 saw a perforation in the rear witness plate, suggesting that a large chunk of material (0.25–0.5 mm depending on the speed, according to Eq. 1) made it through the rear skin. This leads to the suggestion that the MLI layer alone was not sufficient to thoroughly fragment the projectile - unlike what was observed with the Al foil.

3.2. PS targets

On all PS targets, regardless of orientation or front bumper material, perforation occured in the rear Al foil skin. From Fig. 3.6, we find that some of the damage observed within the post-mortem internal structure could only have been the result of secondary ejecta from the impact on a cell (represented as a ghost figure in transparent red). Beyond a 16° dispersion from the point of impact, little to no significant damage can be found. The perforation is clearly the result of a direct hit, yet some ricochet could also have contributed. From Targets 7 and 8, we can narrow down the dispersion from the impact on MLI to <15°, because no significant damage was found beyond that angle. Only part of the damage on the rear skin can therefore be attributed to a direct hit, leading yet again to conclude that internal ricochets were a major factor contributing to rear skin and witness plate damage.

With Target 6 (Fig. 3.7), the orientation of the core at 11° reveals the presence of debris ricochets. Indeed, there is no path for a direct hit to cross the structure and reach the rear skin. Yet, a large hole the size of the open channel is observed, leading to conclude that spalled material and/or ricochets must have found their way there. Moreover, a second point of impact was found on the witness plate, hinting that some of the ricochets found their way through the [110] narrow open channel.

Figure 3.4: Target 4, after impact. Left to right: in chamber, front bumper, rear skin, witness plate

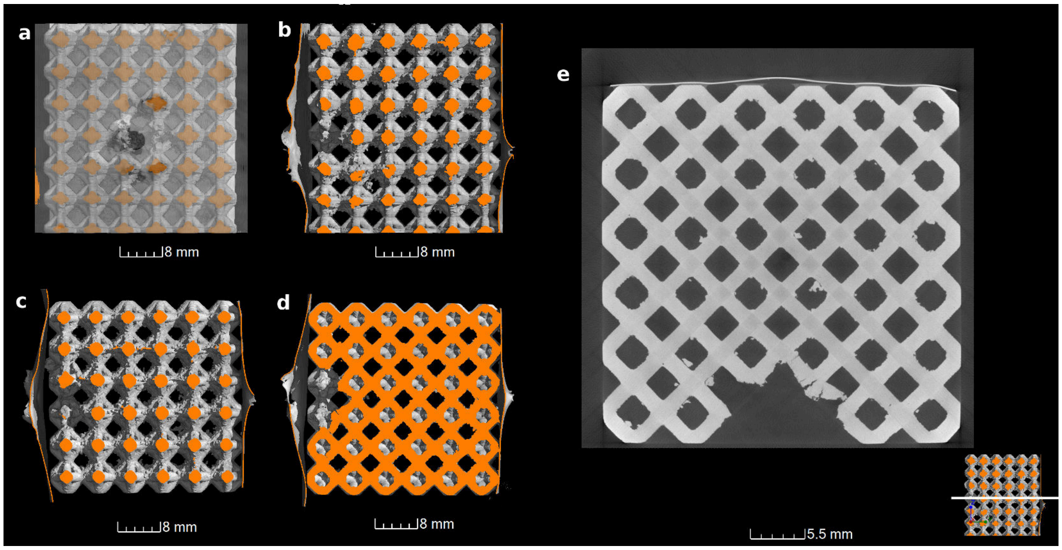

Figure 3.5: Target 4: cutaway images from CT scans. Cross sections are displayed in orange. (a) Front view with transparent bumper. (b) Right view. (c) Top view at exit hole level. (d) Top view at impact level. (e) HD slice of top view at impact level, with visible cracks.

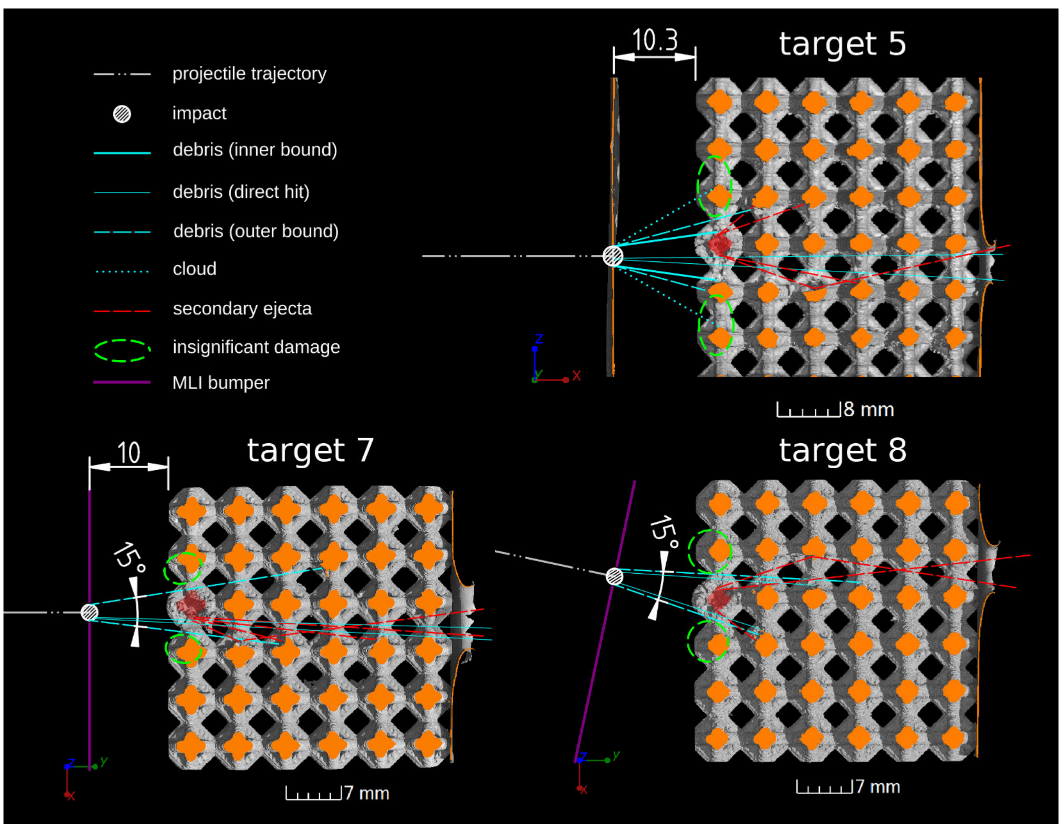

Figure 3.6: Impact model on Targets 5, 7 and 8. Cutaway views from CT scan reconstruction, at impact level. Al foil bumper visible on Target 5. MLI bumpers invisible on CT scans, reproduced for Targets 7 and 8.

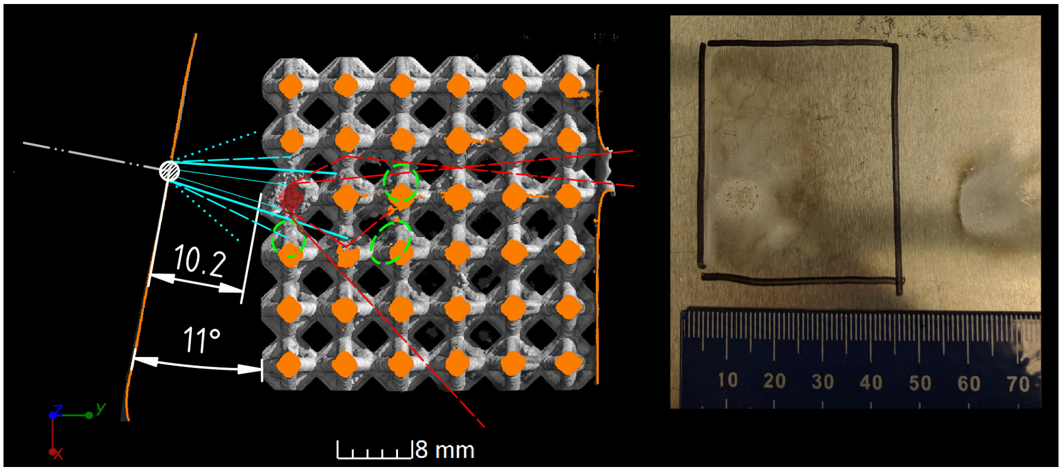

Figure 3.7: Impact model on Target 6. Cutaway top view, at impact level. Witness plate on the right, showing two areas of damage, leading to conclude that part of the ricochets could find a channel in the [110] direction.

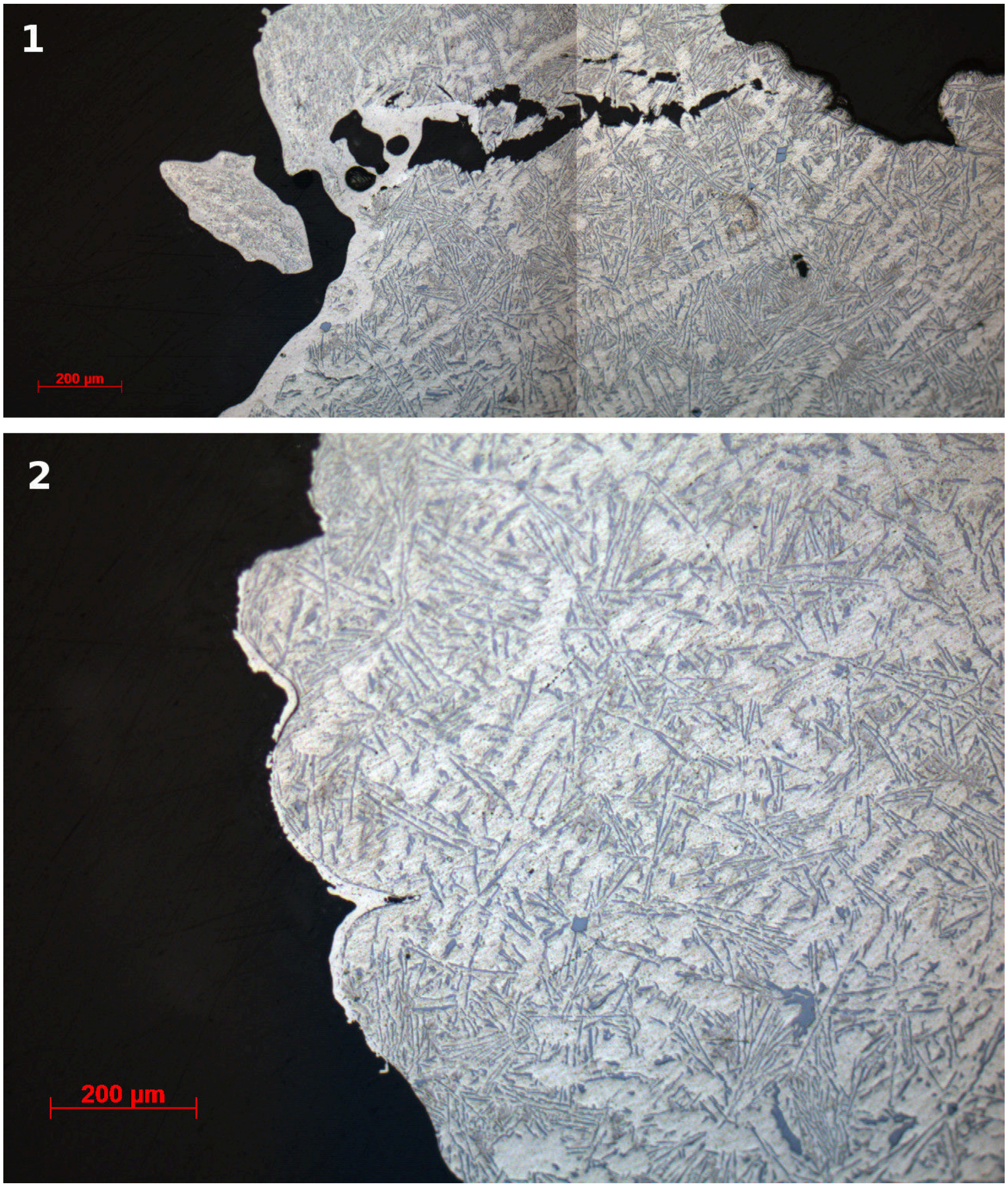

Figure 3.8: (1) Composite view of a wide crack at the forefront of impact. Some 95% Al deposition can be found on the surface and within the crack. (2) 95% Al deposition on the surface of the sample, showing minimal to no damage, as well as no microstructure refinement within the AlSi12 cast alloy.

3.3. SF targets

All three SF targets contained the impact entirely: there was no visible rear plate damage. From visual cues on CT scans, the crater depth can be estimated within a 4–5 mm accuracy; results are shown in Fig. 3.9.

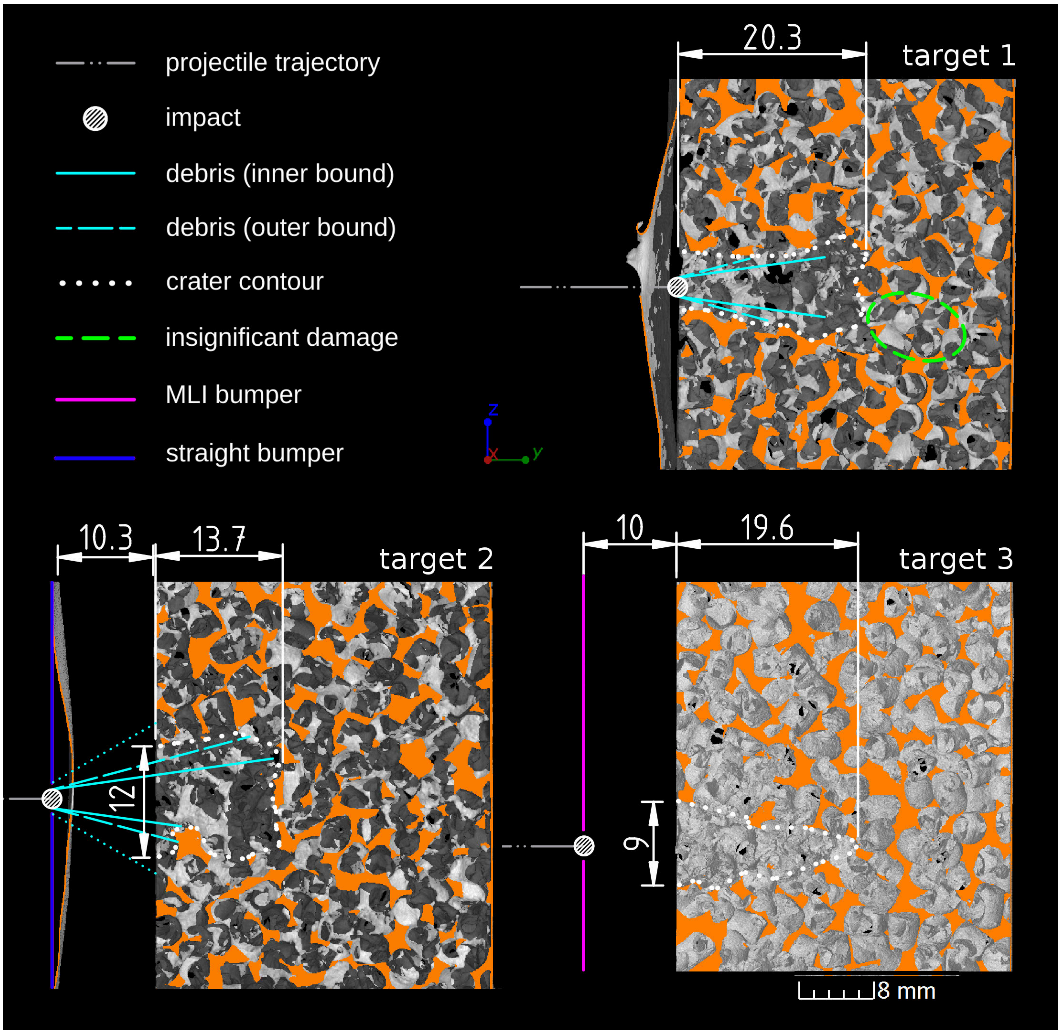

Figure 3.9: Impact models for the SF targets. Cutout view from CT scans, at impact level. The estimated crater depth is indicated. For reference, the impact dispersion is represented following the deductions from PS targets and impact photographs. MLI bumper not visible on CT scans.

Using a MATLAB image processing script on the CT scan slices, we can isolate a $36 \times 36 \times 36$ mm cube situated around the crater, and then divide it into an array of $N{\times}N{\times}N$ smaller cubes (voxels) of volume $V_{voxel} = (36 \text{ mm}/N)^3$. In each of those smaller cubes, the average solid fraction f_S was computed by image analysis. This was accomplished by isolating voxels for which $f_S = 0$ and segregating them into clusters of 6-connectivity, in order to eliminate rogue empty voxels from within the metal foam. The largest cluster was taken to be contained within the crater, and its volume $V_{crater} = n_{voxels} \times V_{voxel}$ was defined as a lower bound on the crater volume.

In this operation, the voxel size has some importance. As the mesh size is refined, more empty voxels begin to fill the empty space within the pores themselves, with the limit at filling the entire empty space within the porous material. With overly coarse voxels, no empty voxel can be found within the sample. Hence, this method was tested over a range of values of N in order to determine the mesh size at which point the crater's apparent volume begins to diverge; this was found to be N=28 or 29 (Fig. 3.10 and 3.11). The crater volume was therefore taken to be the cluster volume at N=27.

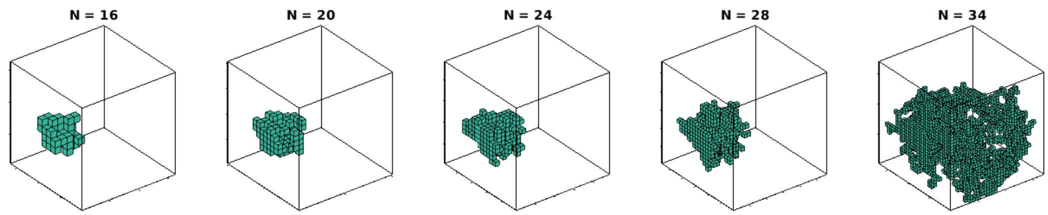

Figure 3.10: Largest 6-connected cluster of empty voxels found within Target 2. The cluster starts filling the undamaged pores above the N=28–29 mark.

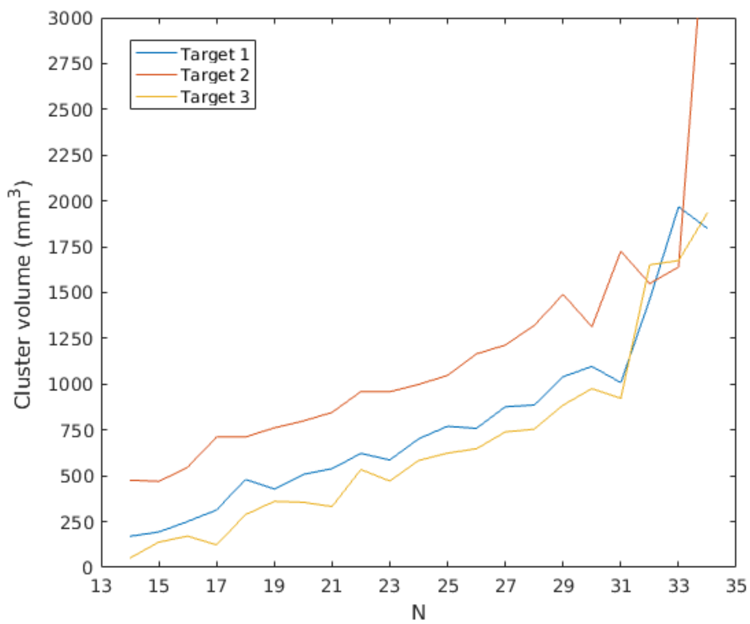

Figure 3.11: Largest 6-connected cluster volume for the three SF targets. The volume diverges above the N=28–29 mark.

Table 3.1 summarizes the principal observations made on crater geometry and average energy dissipation density within the SF cores. The impact energy was estimated based on velocity measurements, assuming a 11.3 mg projectile. To obtain a conservative estimation, it was assumed that 10%

Table 3.1: Estimated crater volume, depth and energy dissipation density in stochastic targets

Target	**1** (foil, against)	**2** (foil, 10 mm)	**3** (MLI, 10 mm)
Crater depth (mm)	20 ± 4	14 ± 4	19± 4
Crater V at N=27 (mm^3)	891	1 297	757
Impact energy (J)	237 ± 12	242 ± 12	245 ± 12
Vol. energy dissipation (J/mm^3)	0.26 ± 0.01	0.18 ± 0.01	0.36 ± 0.01

[3] of the kinetic energy at the muzzle is dissipated from a combination of residual atmospheric drag and the initial impact with the bumper.

In metallography, material of high (95%) Al content from the projectile can be distinguished due to its white, uniform aspect from cast A357 Al-Si, where α-Al appears grayer and contains dark grey flakes (showing up as needles) of precipitated Si. Rather unexpectedly, very little to no damage can be observed in the Al-Si below the surface in most areas coated with projectile debris. Similarly, no significant microstructural refinement, which would be indicative of rapid melting and cooling of Al-Si, was observed. Damage was mostly observed as cracks and torn chunks of cast Al-Si redeposited further. This leads us to conclude that only a minute fraction of displaced material remained within the core, while the majority was lost as larger pieces or dust. This scenario is consistent with the fact that the energy dissipation density is greater for more confined craters such as those in Targets 1 and 3. Indeed for Target 2, the initial spread of the projectile would have led to a greater number of cracked protrusions within the core, the formation of which does not dissipate energy as efficiently as would plastic deformation or melting.

[3]This figure can be justified with a simple model, by considering an inelastic collision between the projectile and a point mass equivalent to a 3 m long, ⌀2 mm column of air at 0.1 Pa, and a 0.15 mm thick, ⌀2 mm disc of aluminium. This corresponds to the matter encountered by the projectile between the muzzle and the core of the target.

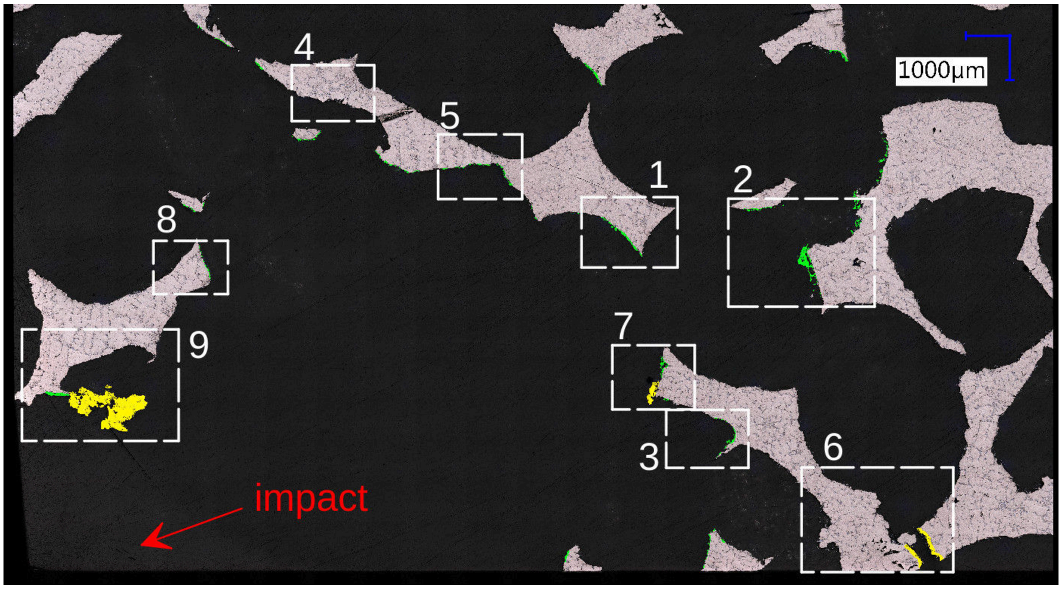

Figure 3.12: Mapping of the principal damage events in SF core. The green coloured areas are (Si-free) deposited layers of 95% Al from the projectile and front bumper. The yellow-coloured areas are of A357 alloy (where Si particles and eutectic can be found) that suffered significant damage. The magnified view of sectors 1-8 are found in the appendix.

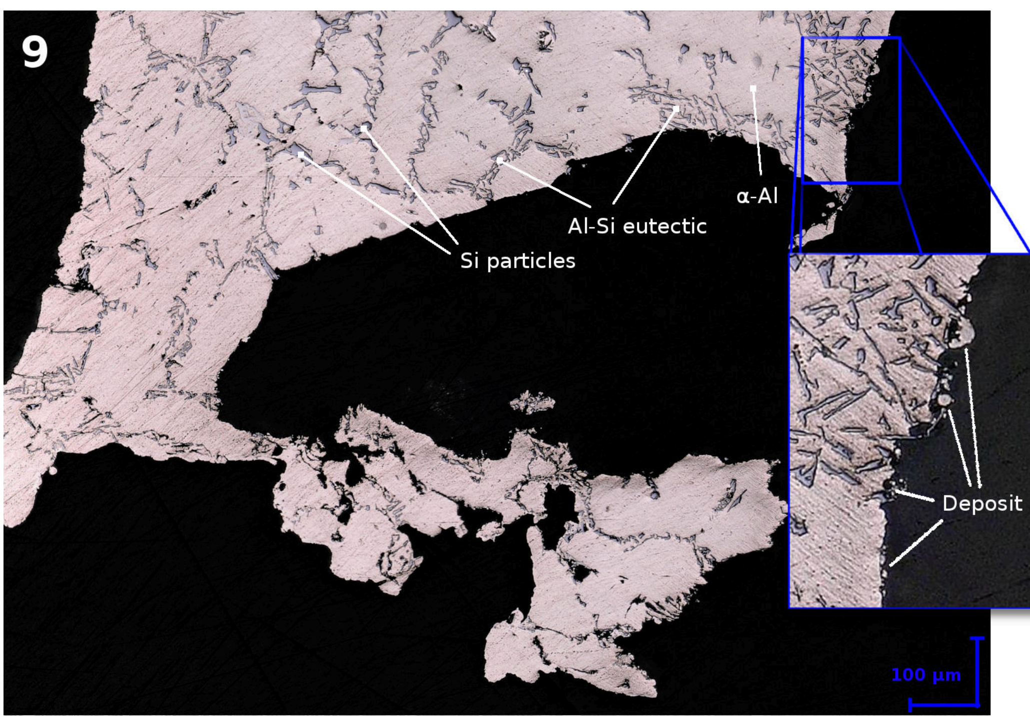

Figure 3.13: Magnified view of Sector 9 as per Fig. 3.12, at the forefront of impact, showing many of the principal features found by microscopy: pristine cast A357, a brighter deposit which appears to be 95% Al debris from the projectile, and a broken-off or deformed A357 chunk.

This said, we note that Target 2 nonetheless performed better in terms of crater depth, which is critical for an efficient shield design. Using crater depth as the critical rear wall thickness for a ⌀2 mm Al projectile at 7 km/s, we can make a comparative assessment of SF vs solid Al plate as a shield's rear wall using Eq. 3 for the simple Whipple shield design; results of the calculation are summarized in Table 3.2. As seen, the Whipple shield design leads to structures having lower weight for equal performance than do SF structures tested here. Using porous metal structures would, therefore, only be justified if some other performance factor were to be included in the analysis. We note, however, that the present testing campaign comprised only three samples, of the same non-optimized material. Given how small (30 percent) the required weight difference is between the two structure types, it is not to be excluded that if the structure (pore shape, pore size, metal alloy) of the stochastic porous metal were to be optimised, it might outperform the Whipple shield structure in terms of impact shielding performance. We thus conclude that porous metals have clear potential in this application, provided – and this is the second key conclusion of this work – that they have no continuous straight channels. In this application, contrary to many other performance criteria (strength, modulus, conductivity, ..), stochastic structures outperform shape-optimized regular periodic truss structures.

Table 3.2: Weight and thickness comparison between SF shields vs. simple Whipple shield of similar performance, using a 0.15 mm Al front bumper. The critical rear wall thickness for SF corresponds to the observed crater depths

	WS, S = 10 mm	SF, S = 10 mm	SF, S = 0 mm
Wall thickness (mm)	2.1 ± 0.2	14 ± 4	20 ± 4
Overall thickness	12.1 ± 0.2	24 ± 4	30 ± 4
Areal weight (g/cm²)	0.60 ± 0.05	0.8 ± 0.2	1.1 ± 0.2

4. Conclusion

A HVIT campaign using a ⌀2 mm Al sphere at velocities ranging from 6.7–7 km/s was conducted on 8 targets made of stochastic foam (SF) or diamond cubic periodically structured (PS) open pores cellular structure as rear walls, and Al foil or MLI as front bumpers.

A major shortcoming of diamond PS cores as HVI shielding material is revealed, namely the fact that open channels in the $< 100 >$ and $< 110 >$ directions allow for the free passage of high-velocity debris, in straight path or altered path by ricochets, passing through the entire structure, for any impact event with incident angles between 0° and 12°, which should concern at least 21% of random incident impacts. Although PS open pore cellular structures offer promising properties as a structural material for space applications, in the context of HVI protection, present results imply that they should always be associated with a more effective shielding material, or only using PS geometries that do not provide open channels.

SF open pore cellular structures were on the other hand able to provide adequate HVI protection, similar to that of simple Whipple shield designs. Porous SF structures tested here were poorer by a factor of 1.3 to 1.9 in terms of areal weight than the simple Whipple shield designs required; however, we note that the structures tested here were not optimized for performance in HVIT testing. Given the number of degrees of freedom available (pore size and shape, relative density, metal composition, ..) there is a good probability that optimized SF metal structures might outperform simple Whipple shield designs in HVIT. This hypothesis has yet to be tested, however.

Metallurgical microscopy on post-mortem samples revealed that the microstructure is not significantly altered by the impact energy where the damage is not already obvious from naked eye inspection or on CT scans.

The spacing between the front bumper and the SF core material played (as expected) a significant role; a 10 mm spacing was found to improve shield performance by about 30% in terms of areal weight compared to a shield with no spacing.

MLI alone as a bumper material was found to perform poorly compared to Al foil of similar areal weight, despite a greater thickness. We suppose that the lamellar structure was not sufficient to efficiently fragment the projectile, and that a combination of adequate spacing between layers, and denser individual layers, might be required to improve MLI performance. Where MLI should be used for its thermal control properties, we suggest it should be associated with Al foil in the context of HVI protection.

In future work, it would be interesting to explore impacts along off-normal axes, and also the performance of microcellular aluminium structures of lower density than those that were explored here. Indeed, the solid fraction of typical aerospace open porosity metal structures in sandwich panels is typically around 8-10%, which is roughly half to a third that of the structures that were tested in the present study. For similar periodic structures of smaller solid fraction, our conclusions can be straightforwardly extrapolated: open channels should still provide pathways for debris and ricochets in regular lattice structures, extending present conclusions to lower density structures of the type investigated here.

For stochastic foams, the presence of protruding so-called “dead weights” or “peninsulas” described in Section 3.3 is a known shortcoming of their manufacturing process. We suggest that reducing their number would likely improve the performance of the shield at fixed density. We note, however, that this may not be a trivial task, as it would involve major changes to a manufacturing process that has been optimized for high-volume, low-cost and low-waste production.

5. Acknowledgements

Our thanks go to Valérie Berger, Hakim Abdulhamid and Cedric Giromini of Thiot Ingénerie for providing us with the hypervelocity impact testing apparatus and the knowledge required to operate it, and to André Guinard of the EPFL LAP, Yannick Delessert of the EPFL SSC, Raphaël Charvet and Cyril Dénéréaz of the EPFL LMM, Robin Amacher of the EPFL DLL and our collegues at the EPFL ATMX workshop for their precious help in this study.

References

[1] Burton G. Cour-Palais. Hypervelocity impact in metals, glass and composites. *International Journal of Impact Engineering*, 5(1):221–237, January 1987.

[2] Eric L. Christiansen. Design and performance equations for advanced meteoroid and debris shields. *International Journal of Impact Engineering*, 14(1):145–156, January 1993.

[3] Michael F. Ashby, Anthony Evans, Norman A. Fleck, Lorna J. Gibson, John W. Hutchinson, and Hayden N.G. Wadley. Metal foams: a design guide - butterworth-heinemann, oxford, uk, isbn 0-7506-7219-6. *Materials and Design*, 23(1):119, 2002.

[4] Russel Goodall and Andreas Mortensen. Porous metals. In David E. Laughlin and Kazuhiro Hono, editors, *Physical Metallurgy (Fifth Edition)*, chapter 24, pages 2399 – 2595. Elsevier, Oxford, 2014.

[5] John W Gehring. Engineering considerations in hypervelocity impact. In Ray Kinslow, editor, *High-Velocity Impact Phenomena*, chapter 9, pages 463–514. Elsevier, 1970.

[6] John Yasensky. Hypervelocity impact evaluation of metal foam core sandwich structures. Technical Report NASA TP-2008-214776, NASA, NASA Johnson Space Center, Houston, 2009.

[7] Shannon Ryan, Troy Hedman, and E.L. Christiansen. Honeycomb vs. foam: Evaluating a potential upgrade to international space station module shielding for micrometeoroids and orbital debris. Technical Report NASA TM–2009–214793, NASA, NASA Johnson Space Center, Houston, 2009.

[8] Shannon Ryan and E.L. Christiansen. Hypervelocity impact performance of open cell foam core sandwich panel structures. Technical Report NASA TM–2015–218593, NASA, NASA Johnson Space Center, Houston, 2015.

[9] Andrew J. Piekutowski. Characteristics of debris clouds produced by hypervelocity impact of aluminum spheres with thin aluminum plates. *International Journal of Impact Engineering*, 14(1):573–586, January 1993.

Appendix A. Close-up on metallographic features

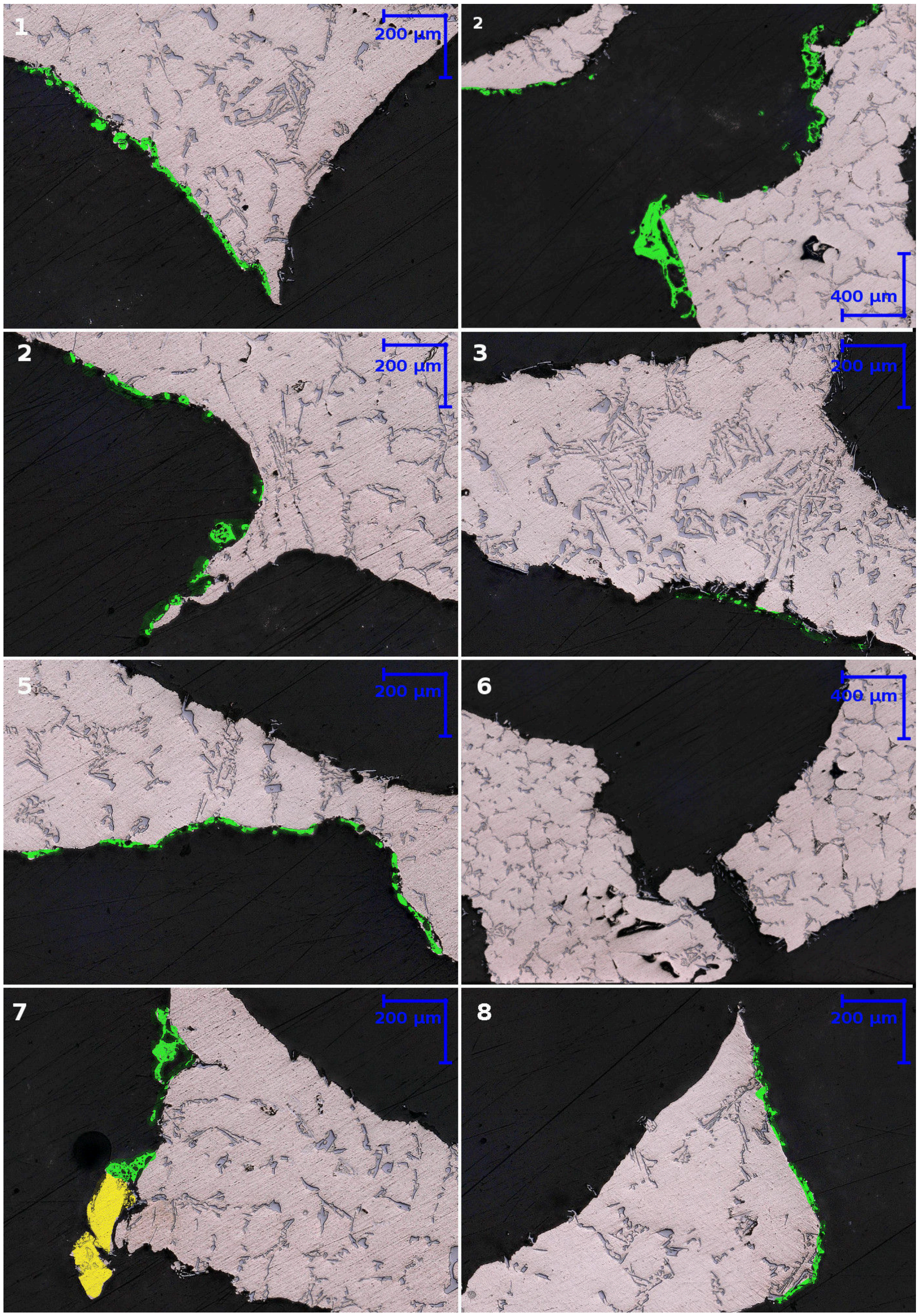

Figure A.1: Magnified view of sectors 1-8 presented in Fig. 3.12.